Tricomponent Brookite/Anatase TiO2/g-C3N4 Heterojunction in Mesoporous Hollow Microspheres for Enhanced Visible-light Photocatalysis

Journal:	*Journal of Materials Chemistry A*
Manuscript ID	TA-ART-01-2018-000386.R1
Article Type:	Paper
Date Submitted by the Author:	19-Mar-2018
Complete List of Authors:	Wei, Hao; The University of Melbourne, School of Chemistry McMaster, William; The University of Melbourne, School of Chemistry Tan, Jeannie; The University of Melbourne, School of Chemistry Chen, Dehong; Australian National University, ; Caruso, Rachel; RMIT University, School of Science; The University of Melbourne, Chemistry

SCHOLARONE™
Manuscripts

Journal Name

ARTICLE

Tricomponent Brookite/Anatase TiO₂/g-C₃N₄ Heterojunction in Mesoporous Hollow Microspheres for Enhanced Visible-light Photocatalysis

Hao Wei,[a] William A. McMaster,[a] Jeannie Z. Y. Tan,[ab] Dehong Chen*[c] and Rachel A. Caruso*[ad]

The three major polymorphs of TiO₂, anatase, rutile, and brookite, are widely utilised to form heterojunction semiconductors for superior photocatalytic performance due to their unique optical properties and tunable morphologies. Mesoporous brookite/anatase TiO₂/g-C₃N₄ hollow microspheres were prepared from pre-made, amorphous TiO₂ microspheres via a facile nanocoating procedure and showed mixed phases of brookite (48 %), anatase (44 %), and rutile (8 %). The mesoporous hollow microspheres exhibited a unique shell morphology of packed TiO₂/g-C₃N₄ nanosheets, porosity with pore volume of 0.20 cm³ g⁻¹ and surface area of 37.1 m² g⁻¹. Compared with mesoporous g-C₃N₄, the composite hollow microspheres coated with 10 wt% g-C₃N₄ were 5-fold more active in degrading phenol under visible light irradiation. In contrast with mesoporous pristine anatase or rutile TiO₂/g-C₃N₄ composites, the photocatalytic activity was improved for the multiphase TiO₂/g-C₃N₄ material due to the more negative conduction band, which benefitted electron transfer. A mechanism for the enhanced photocatalytic behaviour was proposed for the mesoporous brookite/anatase/rutile TiO₂/g-C₃N₄ hollow microspheres, showing that the multicomponent heterojunction could enhance the photocatalytic properties in the visible range.

1 Introduction

Of the many transition metal oxides, titanium dioxide (TiO₂) is one of the most studied because of its abundance, structural diversity and numerous potential applications such as photocatalysis, solar cells, white pigments and protective coatings.[1-3] Among various applications, photodegradation of organic pollutants has become essential due to soaring global population, industrial activity and energy consumption.[4, 5] As a photocatalyst, TiO₂ is a wide band gap semiconductor (3.2 eV) that can be used to decompose organic compounds under ultraviolet (UV) irradiation, and occurs mainly in three different phases: anatase (tetragonal, space group $I4_1/amd$), rutile (tetragonal, space group $P4_2/mnm$) and brookite (orthorhombic, space group $Pbca$).[6] Of the three, the brookite phase is the least studied because of its thermodynamic metastability (< 600 °C) and the difficulties encountered in its synthesis.[7-9] However, for TiO₂ particles 11-35 nm in size, brookite is more stable than anatase, exhibiting a more negative flat band potential that is beneficial to photocatalytic performance in both CO₂ photoreduction and dye photodegradation.[10] Due to its intrinsic band gap, TiO₂ suffers from a low solar energy conversion efficiency and a high

recombination rate of photogenerated electron-hole pairs.[4, 9, 11] Numerous attempts, including the introduction of interior states by metal[12, 13] or non-metal dopants,[14, 15] or through heterojunction semiconductor formation,[16-20] have been made to extend the photoresponse range of TiO₂ to the visible light region for practical applications. Tuning the morphology and porosity can provide abundant pathways for mass transfer and light harvesting.[21, 22] Recently, titanium carbides and sulphides were developed as efficient visible light photocatalysts, demonstrating improved performance in hydrogen production.[23, 24]

Graphitic carbon nitride (g-C₃N₄), a non-metal semiconductor, has been widely investigated due to its narrow band gap (2.69 eV) and high chemical stability for decomposing organic pollutants under visible light irradiation.[25-27] The negative potential (-1.12 eV vs. NHE) of the lowest unoccupied molecular orbital of g-C₃N₄ results in heterojunction formation when combined with TiO₂ polymorphs.[28, 29] When TiO₂ and g-C₃N₄ are in intimate contact, a type-II heterojunction is formed at the interface. As a result, the conduction band (CB) and valence band (VB) positions are staggered by lattice conjugation between the two semiconductors for charge transfer.[30] Recently, N-TiO₂/g-C₃N₄ nanofibers, which were prepared by electrospinning combined with a modified thermal oxidation process, demonstrated enhanced photocatalytic activity based on the heterojunction sensitization effect. However, the limited light-harvesting capability of the fibres under solar light reduced the water decomposition efficiency for H₂ conversion.[31] In a different approach, heterojunctions formed after g-C₃N₄ nanosheets were grafted onto TiO₂(B) nanofibers via a solid-state reaction at high temperature. Benefitting from the

a. Particulate Fluids Processing Centre, School of Chemistry, The University of Melbourne, Victoria 3010, Australia.
b. CSIRO, Manufacturing, Clayton South, Victoria 3169, Australia.
c. Australian National University, Canberra, ACT 2601, Australia.
d. RMIT University, Melbourne, Victoria 3000, Australia
† Electronic Supplementary Information (ESI) available. See DOI: 10.1039/x0xx00000x

alignment between the g-C_3N_4 and TiO_2(B) planes, the composite delivered higher visible-light photoactivity in degrading organic dye than either pristine TiO_2(B) or g-C_3N_4.[30]

Tunable morphologies are crucial to enhance mass transfer and light-harvesting, which can improve photocatalytic performance.[32-34] Compared with solid structures, hollow shells exhibit low density and high light-harvesting efficiency, resulting in enhanced photocatalytic properties.[15, 17] High porosity is another factor that enables fast transport and diffusion of molecules to and from active sites. Moreover, simply increasing the size of the mesoporous microsphere, e.g. > 1 μm, does not benefit light harvesting and mass transfer.[21] Accordingly, control over both mesoporosity and nanoscale properties will improve photocatalytic performance in decomposing organic molecules.

Unlike anatase and rutile, brookite TiO_2 nanostructures have been rarely studied as photocatalysts, either in the single phase or as heterojunctions coupled with other semiconductors.[8, 10, 35, 36] In our previous report, mesoporous anatase TiO_2/g-C_3N_4 microspheres were prepared via solvothermal treatment without NaCl addition.[37] However, those microspheres neither contained brookite, nor featured a hollow structure. Hence, mesoporous brookite/anatase TiO_2/g-C_3N_4 hollow microspheres were prepared via a nanocoating procedure in order to take advantage of the particle size metastability of brookite/anatase mixed phases, visible light activity of g-C_3N_4, and beneficial properties of porous, hollow structures. Premade, mesoporous brookite/anatase TiO_2 hollow microspheres were mixed with aqueous cyanamide solution, then the organic precursor was polymerized to a g-C_3N_4 layer coated onto the TiO_2 surface by calcination. The mesoporous brookite/anatase TiO_2/g-C_3N_4 hollow microspheres exhibited a unique fluffy hollow structure with abundant mesopores. Moreover, due to the TiO_2/g-C_3N_4 heterojunctions, a 5-fold increase in photocatalytic performance was achieved when degrading phenol under visible light irradiation. Based on the characterization of composition, morphology, optical and electronic properties, a mechanism was proposed for the role of the tricomponent brookite/anatase TiO_2/g-C_3N_4 heterojunction in the enhanced photocatalytic degradation of phenol in the visible range.

2 Experimental details

2.1 Chemicals

Titanium (IV) isopropoxide (TIP, 97 %), cyanamide (H_2NCN, AR), *tert*-butyl alcohol (*t*-BuOH, > 99.0 %), hexadecylamine (HDA, 90 %), ethylenediaminetetraacetic acid disodium salt (EDTA-2Na, AR), Pluronic P123 triblock copolymer ($EO_{20}PO_{70}EO_{20}$), tetraethyl orthosilicate (TEOS, 98 %), and ammonium bifluoride (NH_4HF_2, AR) were purchased from Sigma-Aldrich. Absolute ethanol (> 99.5 %), phenol (AR), 1-butanol (99.8 %), formaldehyde solution (25 wt%, AR) and sodium chloride (NaCl, AR) were purchased from Chem-Supply. Hydrochloric acid (HCl, 32 wt%, Merck), ammonia solution (25 wt%, Merck) and ammonium chloride (NH_4Cl, AR, BDH) were also used. All reagents were used as received. Milli-Q water was collected from a Millipore academic purification system with a resistivity higher than 18.2 MΩ·cm.

2.2 Material synthesis

Synthesis of Mesoporous Brookite/Anatase TiO_2 Hollow Microspheres (MBA)

Amorphous TiO_2 microspheres were prepared in ethanol via a sol-gel procedure with HDA as the structure directing agent.[38] Typically, HDA (7.95 g) was dissolved in ethanol (800 mL) with aqueous NH_4Cl solution (3.2 mL, 0.1 M). Under vigorous stirring, TIP (13.57 mL) was added quickly and stirred for 10 s. After keeping static for at least 12 h, the white precipitate was collected at 5000 rpm for 10 min by centrifugation (Beckman Coulter Allegra 25R centrifuge) and washed with ethanol 3 times. The amorphous microspheres were dried at room temperature.

Solvothermal treatment in the presence of ammonia and NaCl was performed to prepare the mesoporous brookite/anatase TiO_2 hollow microspheres. Typically, amorphous TiO_2 microspheres (1.6 g) were dispersed in a solution of ethanol (10 mL), ammonia (50 mL) and NaCl (2.4 g) followed by stirring for 30 min at room temperature. The suspension was sealed in a Teflon-lined steel autoclave (100 mL) and heated at 160 °C for 16 h. The resultant TiO_2 powder was recovered by centrifugation at 5000 rpm for 10 min and then washed with ethanol and water 3 times. To exchange the sodium ion, samples were redispersed in dilute HCl (0.2 M, 50 mL) at 30 °C for 3 h, which was then brought to neutral pH by the addition of water. The ion exchange process was repeated 3 times to remove the sodium ions. The final MBA samples were obtained after calcination at 550 °C for 6 h in air (Bel Tetlow K2 chamber furnace with Shimaden FP93 controller).

Synthesis of Mesoporous Anatase and Rutile TiO_2 Hollow Microspheres (MA and MR)

Amorphous TiO_2 microspheres (2 μm) were prepared in *t*-BuOH via a sol-gel procedure with HDA as the structure directing agent.[21] Typically, HDA (11.92 g) was dissolved in 1-butanol (600 mL) at room temperature followed by the addition of aqueous NH_4Cl solution (0.1 M, 4.8 mL). Under vigorous stirring, TIP (13.57 mL) was added quickly and stirred for 60 s. The solution was kept static for 18 h, then the white precipitate was collected by centrifugation and washed with ethanol 3 times. The as-prepared amorphous microspheres were dried at room temperature.

Solvothermal treatment was performed to prepare mesoporous anatase and rutile TiO_2 hollow microspheres. Typically, amorphous TiO_2 microspheres (1.6 g) were dispersed in a mixed solution of water (5 mL) and ammonia (25 mL) and stirred for 30 min at room temperature. The mixture was heated in a Teflon-lined autoclave (50 mL capacity) at 160 °C for 48 h. Mesoporous anatase and rutile TiO_2 microspheres were obtained after calcination at 550 °C and 750 °C for 4 h in air, respectively.

Synthesis of Mesoporous Brookite/Anatase, Anatase or Rutile TiO_2/g-C_3N_4 Hollow Microspheres (MBACN, MACN or MRCN)

MBA (0.8 g) was dispersed in aqueous cyanamide solution (0.8 g mL^{-1}, *x* ml) and kept stirring at room temperature until the solvent had evaporated completely. After calcination at 550 °C

for 4 h in a nitrogen atmosphere with a ramp rate of 1 °C min^{-1}, mesoporous brookite/anatase TiO$_2$/g-C$_3$N$_4$ hollow micro-spheres were obtained (denoted as MBACN-x, where x was the volume of aqueous cyanamide solution).

To obtain mesoporous anatase and rutile TiO$_2$/g-C$_3$N$_4$ hollow microspheres, MA or MR (0.8 g) was dispersed in aqueous cyanamide solution (0.8 g mL^{-1}, 2 mL), followed by drying and calcination (as detailed in the previous paragraph). The corresponding composite hollow microspheres were labelled as MACN-2 and MRCN-2.

Synthesis of the Ordered Mesoporous g-C$_3$N$_4$ (CN)

The ordered mesoporous silica SBA-15 was introduced as a hard template with CN fabricated via a nanocasting procedure.[39] Typically, SBA-15 (0.5 g) was dispersed in an aqueous cyanamide solution (0.8 g mL^{-1}, 1 ml), and kept stirring until the solvent had evaporated completely. Next, a silica/carbon nitride composite was obtained after calcination at 550 °C for 4 h in nitrogen. The template was removed by dissolution in aqueous NH$_4$HF$_2$ solution (1 M) for at least 8 h to obtain the final CN, before washing in an ethanol/water mixture (1:1) 3 times and drying at 80 °C.

2.3 Material Characterization

Scanning electron microscopy (SEM) was performed on a Quanta 200F FEI scanning electron microscope at an accelerating voltage of 15 kV and without Au coating. Transmission electron microscopy (TEM) and high-resolution TEM (HRTEM) were conducted at 200 kV on an FEI Tecnai F20 transmission electron microscope. Powder X-ray diffraction (XRD) patterns were acquired on a Bruker D8 Advance Diffractometer using Cu Kα radiation. The diffractometer was set at 40 kV and 40 mA as working parameters, with samples scanned from 5° to 80° 2θ. Thermogravimetric analysis (TGA) was conducted on a Mettler Toledo TGA/SDTA851e thermogravimetric analyser heating from 25 °C to 900 °C with a ramp of 10 °C min^{-1} under oxygen flow (30 mL min^{-1}). Nitrogen sorption isotherms were measured at -196 °C using a Micromeritics TriStar 3000 Surface Area and Porosity Analyser. Prior to measurement, calcined samples were degassed at 150 °C for at least 8 h on a vacuum line. Specific surface areas were calculated by a standard multipoint Brunauer-Emmett-Teller (BET) method using adsorption values in the range P/P$_0$ = 0.05–0.20. The Barrett-Joyner-Halenda (BJH) model was applied to the adsorption branch of the isotherm to determine pore size distributions, while total pore volume was estimated from the adsorbed N$_2$ amount at P/P$_0$ = 0.983. UV-visible diffuse reflectance spectra were collected on a PerkinElmer Lambda 1050 UV/Vis/NIR spectrophotometer with an integrating sphere accessory for λ = 200–800 nm. Fourier transform infrared spectra (FT-IR) were obtained using a FT-IR spectrometer (Varian 7000) with an attenuated total reflectance accessory, collecting in a range from 400 cm^{-1} to 4000 cm^{-1}. Samples were dried in vacuum at 90 °C for at least 24 h before testing. X-ray photoelectron spectroscopy (XPS) data were recorded on a VG ESCALAB 220i-XL spectrometer equipped with a twin crystal monochromated Al Kα X-ray source, which emitted a photon energy of 1486.6 eV at 10 kV and 22 mA. The C 1s peak at 285 eV was used as a reference for the calibration of the binding energy scale. Photoluminescence (PL) spectra were measured on a Varian Cary-Eclipse at room temperature for λ = 350–600 nm using an excitation wavelength of 325 nm. Electron paramagnetic resonance (EPR) spectra were recorded on a Bruker Elexsys E500 spectrometer with a Bruker ER 4122SHQ cavity by applying an X-band microwave (9.43 GHz, 1 mW) with sweeping magnetic field (600 G). Samples were cooled to 77 K in liquid nitrogen, and the g factor was calibrated by reference to DPPH (1,1-diphenyl-2-picrylhydrazyl, g = 2.000).

2.4 Evaluation of Photocatalysts

Photocatalysis experiments were conducted in a fume cupboard in a dark room to avoid light exposure. The photocatalytic performance was evaluated by analysing the degradation of aqueous phenol (10 ppm, 160 mL) in the presence of the photocatalyst (80 mg) under visible light irradiation in a water-jacketed chamber. Prior to irradiation, the suspension was sonicated in a sonication bath for 5 min then equilibrated by intense stirring in the dark for 1 h to obtain phenol adsorption/desorption equilibrium. The chamber was kept at 20 ± 1 °C and continuously bubbled with air at a flow of 5 bubbles s^{-1} (gas code: 052, BOC) during equilibration and degradation. A 500 W Hg (Xe) globe (Oriel) with a Schott filter (cut-off λ < 420 nm) was used as the visible light source (light intensity: 8.5 mW cm^{-2}). Phenol degradation was monitored by taking 3 mL aliquots after 0 min, 15 min, 30 min, 45 min, and 60 min irradiation, collecting the supernatant by centrifugation (Hermle Z 233 M-2) at 15,000 rpm for 15 min, then determining the concentration of phenol from the characteristic absorption peak at λ = 270 nm from a spectrum (λ = 200–500 nm) obtained using a quartz cuvette on a UV/Vis/NIR spectrophotometer (Lambda 1050, PerkinElmer).

The active species generated in the photocatalytic system were detected through trapping tests by EDTA-2Na and t-BuOH.[40] Trapping tests were conducted under the same conditions as the photocatalysis experiments. EDTA-2Na (2.92 g, 10 mmol) or t-BuOH (1 mL, 10 mmol) was added to the aqueous phenol solution and photocatalyst prior to sonication. All photocatalysis experiments were repeated 5 times with controlled parameters for reproducibility.

3 Results and discussion

Amorphous TiO$_2$ microspheres were prepared via a sol-gel process in the presence of HDA, from which mesoporous brookite/anatase TiO$_2$ hollow spheres (MBA) were obtained via a solvothermal process followed by calcination. To build a heterojunction with g-C$_3$N$_4$, aqueous cyanamide solution was introduced as an organic precursor, which infiltrated the MBA and formed a thin layer during calcination under an inert nitrogen atmosphere. The final mesoporous brookite/anatase TiO$_2$/g-C$_3$N$_4$ hollow microspheres were labelled MBACN-x,
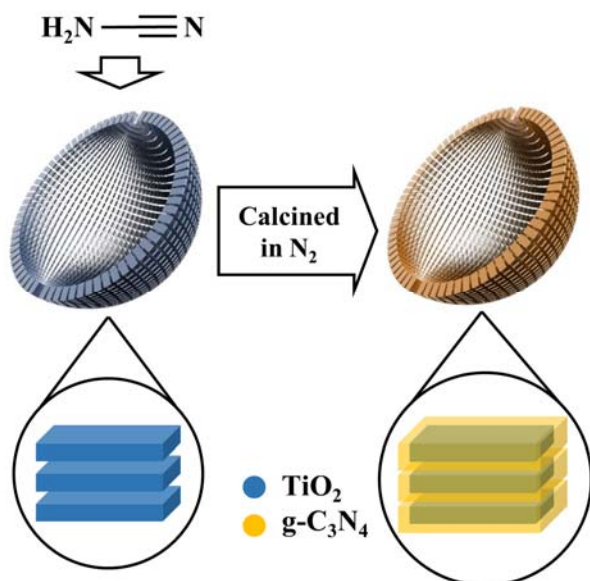
Scheme 1 Schematic of the nanocoating strategy of MBACN-*x* (depicted as a hemisphere shell to show the internal and external surfaces).

where *x* indicates the 1, 2, or 3 mL of cyanamide solution used during synthesis (Scheme 1). As references, mesoporous anatase TiO_2 and mesoporous rutile TiO_2 hollow spheres were fabricated by a similar process, with corresponding mesoporous TiO_2/g-C_3N_4 hollow microspheres labelled as MACN-2 and MRCN-2, respectively, obtained after the infiltration of aqueous cyanamide solution (2 mL).

After different amounts of cyanamide were mixed with the white MBA powder (Fig. S1a), the composite microspheres revealed the unique colors of yellow, orange, and dark orange, resulting from the thin g-C_3N_4 layer coated on the TiO_2 substrate (Fig. S1b-d). This coloration was in keeping with the yellow of ordered mesoporous g-C_3N_4 (CN), which was prepared by the infiltration and then calcination of cyanamide inside of an ordered mesoporous silica (SBA-15) template followed by removal of the template (Fig. S1e). The morphologies of the MBA and MBACN-2 microspheres were observed by SEM, each had a uniform diameter of 1 μm (Fig. 1a and c). After infiltration with aqueous cyanamide solution and thermal conversion to g-C_3N_4, the morphology of MBACN-2 remained the same as the raw MBA microspheres, being without obvious aggregation on the surface. This was also the case for MBACN-1 (Fig. S2a). At higher magnification (Fig. 1b and d), the open structure built of nanosheets was maintained after coating with g-C_3N_4. However, with a higher amount of cyanamide infiltrated into MBA (i.e. MBACN-3), aggregation of g-C_3N_4 was found in the calcined composite (Fig. S2b). Using a solvothermal process without the addition of NaCl, pristine anatase TiO_2 and rutile TiO_2 hollow microspheres were coated with g-C_3N_4 (MACN-2 and MRCN-2, respectively). These microspheres were of a larger diameter (2 μm) than MBACN-*x* and had smoother surfaces packed by TiO_2 nanocrystals without observable nanosheet morphology (Fig. 1e and f).

The TEM of MBA showed a hollow structure composed of TiO_2 nanosheets (Fig. 2a). From HRTEM, the crystal structure of
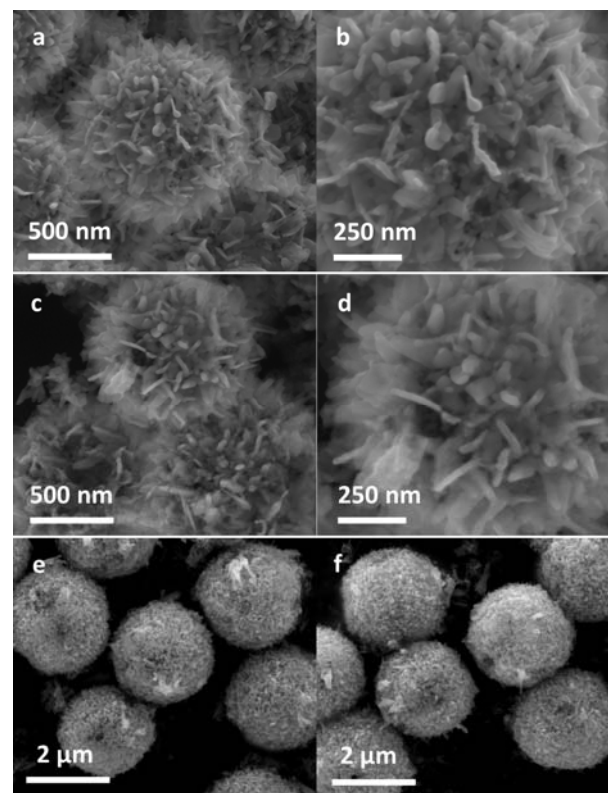

Fig. 1 SEM images of a, b) MBA, c, d) MBACN-2, e) MACN-2, and f) MRCN-2.

brookite TiO_2 and anatase TiO_2 were observed after the solvothermal process with lattice fringes of 2.9 Å and 3.52 Å indexed to the (121) plane of brookite TiO_2 and (101) plane of anatase TiO_2, respectively (Fig. 2b). The lattice conjugation between the different TiO_2 phases exhibited a special angle, which allowed close contact and efficient charge transfer through the interface. TEM of the g-C_3N_4 composite hollow microsphere MBACN-2 exhibited a similar structure to MBA, without obvious g-C_3N_4 aggregation (Fig. 2c), which was in keeping with SEM observations (Fig. 1). HRTEM of the composite nanosheets revealed that brookite/anatase TiO_2 and g-C_3N_4 were in close contact at the interface, showing clear boundaries between the domains (Fig. 2d and S2c). Benefitting from the hydrophilicity of the TiO_2 substrate, the aqueous cyanamide solution formed a thin coating layer of g-C_3N_4 after thermal polymerization without aggregation.[28] The lattice fringes of 2.90 Å, 3.52 Å, and 3.36 Å were indexed to the (121) plane of brookite TiO_2, (101) plane of anatase TiO_2 and the (002) plane of g-C_3N_4, respectively, indicating that the lattices of the three components had formed a heterojunction.

TGA curves of MBA, MBACN-*x*, MACN-2, and MRCN-2 obtained under an oxygen atmosphere are shown in Fig. 3a. A small mass loss (< 2 wt%) occurred in all composites below 400 °C, which was attributed to the decomposition of *s*-triazine moieties and poorly polymerized melem.[41] Calculating the difference in mass loss between MBA and MBACN-*x* after combustion at 500 °C, the g-C_3N_4 content of MBACN-1, MBACN-2, and MBACN-3 was approximately 3.2 wt%, 9.8 wt%, and 16.3 wt%, respectively. With the same volume of cyanamide added during the synthesis, MACN-2 and MRCN-2 showed mass losses of 10.2
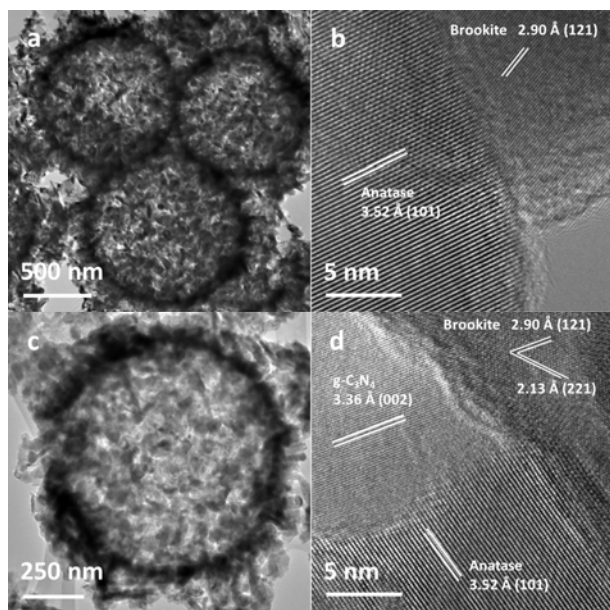
Fig. 2 TEM images of a) MBA and c) MBACN-2, and HRTEM images of b) MBA and d) MBACN-2.

wt% and 12.5 wt% at 500 °C, possibly due to different polymerization of the precursor. Across the entire temperature range, mass loss from MBA was negligible, due to either adsorbed moisture or surface hydroxyl groups (Fig. 3a). XRD patterns of MBA and MBACN-*x* (Fig. 3b) exhibited well defined peaks at 25.3°, 30.9°, 36.2°, 37.8°, 40.1°, 42.3°, 48.0°, 54.2°, 55.1°, and 62.1° that were indexed to the (120), (121), (012),

(201), (022), (221), (231), (320), (241), and (052) crystal planes of brookite TiO_2 (JCPDS Card No. 29-1360) with some peaks also corresponding to anatase TiO_2 (JCPDS Card No. 21-1272) and rutile TiO_2 (JCPDS Card No. 21-1276). The crystal size (approximately 28.3 nm, Table S1) calculated from the (120) peak of MBACN-*x* by the Scherrer equation was not obviously changed compared with pristine TiO_2 (MBA), implying no significant crystal growth during the g-C_3N_4 nanocoating process. Additionally, no peaks of g-C_3N_4 were identified in the composites, due to the low organic content, unlike CN which was entirely composed of g-C_3N_4 (Fig. 3b). Rietveld refinement of MBA and MBACN-2 indicated that the brookite, anatase, and rutile contents of the TiO_2 phases remained almost the same after g-C_3N_4 nanocoating and thermal treatment (Fig. S3a and b). Brookite increased from 46 % to 48 %, anatase dropped from 46 % to 44 % and rutile was unchanged at 8 %. In contrast, MACN-2 and MRCN-2 were pristine anatase TiO_2 and rutile TiO_2, respectively, after the g-C_3N_4 coating procedure (Fig. S3c).

Nitrogen sorption isotherms (Fig. 3c) of MBA and MBACN-*x* featured type IV adsorption branches with H2 hysteresis loops, due to disordered interparticle pores.[38] MBA had a broad distribution of mesopore diameters distinctly centred at 17.8 nm, extending to small pore sizes of 2-5 nm (Fig. 3d and Table 1). After coating with a g-C_3N_4 layer, the mesopore size distributions broadened and became less distinct, which was ascribed to small TiO_2 mesopores (2-5 nm) being coated and/or blocked by g-C_3N_4. Moreover, the surface area decreased gradually from 49.2 m^2 g^{-1} to 30.3 m^2 g^{-1}, while the pore volume
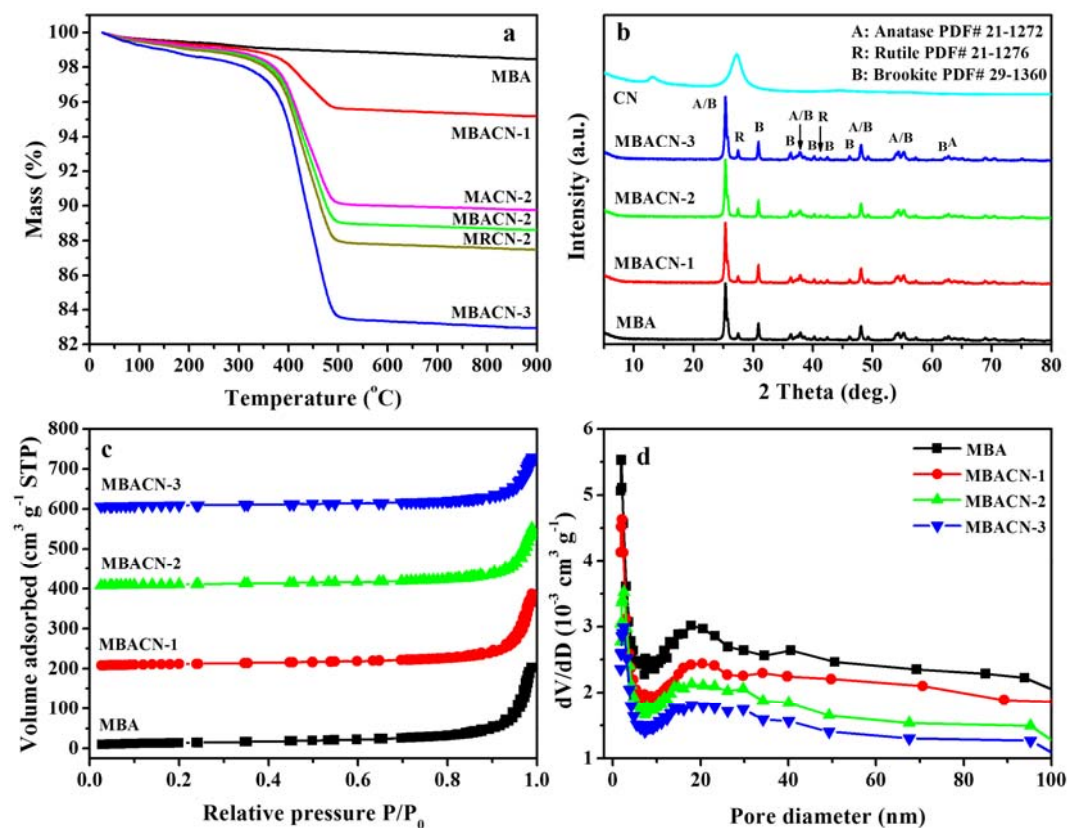

Fig. 3 a) TGA curves of MBA, MBACN-*x*, MACN-2, and MRCN-2. b) XRD patterns of MBA, MBACN-*x* and CN. c) Nitrogen sorption isotherms and d) BJH pore size distributions of MBA and MBACN-*x*. The isotherms of MBACN-*x* are offset vertically by 200 cm^3 g^{-1}, 400 cm^3 g^{-1}, and 600 cm^3 g^{-1}.

followed a similar trend from 0.25 cm^3 g^{-1} to 0.16 cm^3 g^{-1} as the volume of cyanamide used during synthesis was increased (Table 1). Nitrogen sorption isotherms of MACN-2 and MRCN-2 (Fig. S4a) were similar to MBA and MBACN-x, yet, by contrast, MACN-2 displayed a dual pore structure with a small distribution centred at 34.4 nm, including a mesoscale distribution centred at 14.7 nm and a broad peak at 81.3 nm for macropores (Fig. S4b and Table 1). A single broad distribution from 10 nm to 90 nm centred at 50.5 nm was observed in MRCN-2 (Fig. S4b) as a higher temperature (750 °C) calcination was used to obtain rutile TiO$_2$ (MR). In addition, MRCN-2 had the lowest surface area (18.2 m^2 g^{-1}) and pore volume (0.12 cm^3 g^{-1}) among all composite samples, due to temperature-induced TiO$_2$ crystal growth.

Table 1. Physical properties of MBA, MBACN-x, CN, MACN-2, and MRCN-2.

Sample	Pore size[a] (nm)	Surface area (m^2 g^{-1})	Pore volume (cm^3 g^{-1})
MBA	17.8	49.2	0.25
MBACN-1	20.4	41.4	0.23
MBACN-2	18.0	37.1	0.20
MBACN-3	18.0	30.3	0.16
CN	14.6	45.8	0.29
MACN-2	14.7/34.4	45.8	0.29
MRCN-2	50.5	18.2	0.12

a) Peak of the pore size distribution.

The FT-IR spectra of MBA, MBACN-x and CN indicated the presence of different organic species (Fig. S5). The pristine TiO$_2$, MBA, had a wide absorption band at 500-900 cm^{-1} that was attributed to Ti-O stretching. Mesoporous g-C$_3$N$_4$, CN, showed a strong absorption peak at 807 cm^{-1} associated with the breathing mode of s-triazine units belonging to g-C$_3$N$_4$, as well as multiple peaks from 1240-1600 cm^{-1} that were attributed to aromatic C-N stretching vibrational modes.[39] Owing to their higher organic content, the stronger peaks of the aromatic C-N vibrations were identified in MBACN-2 and MBACN-3, but the s-triazine peak at 807 cm^{-1} could not be identified due to its low intensity and overlapping from the TiO$_2$ signal.

The light absorption properties of MBA, MBACN-x, MACN-2, MRCN-2, and CN were characterized by UV-visible diffuse reflectance spectroscopy (Fig. 4a). The light absorption of MBA was confined to wavelengths lower than 400 nm; however, the infiltration of g-C$_3$N$_4$ significantly altered this, with each composite material exhibiting light absorption that extended through the entire visible range. Additionally, for the composites, the absorbance was higher than for CN for wavelengths above 450 nm, demonstrating enhanced response in the visible range. (Fig. 4a). To examine the separation of photogenerated charge carriers, PL spectra of selected samples were obtained (Fig. 4b). Band-band emission and excitonic fluorescence due to surface oxygen vacancies and defects are associated with the peaks in the MBA and MRCN-2 spectra below 415 nm (Fig. S6), whereas the intense, broad peak of CN centred at 460 nm (Fig. 4b) indicated a high recombination rate of electron−hole pairs. MBACN-2 and MACN-2 had insignificant peaks across the entire PL range, implying the occurrence of fast and efficient separation of electron−hole pairs, the importance
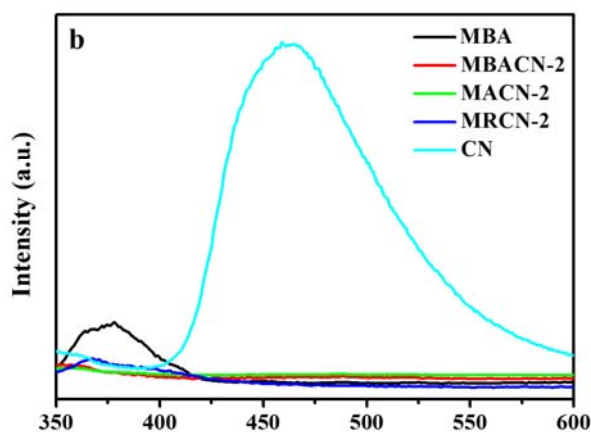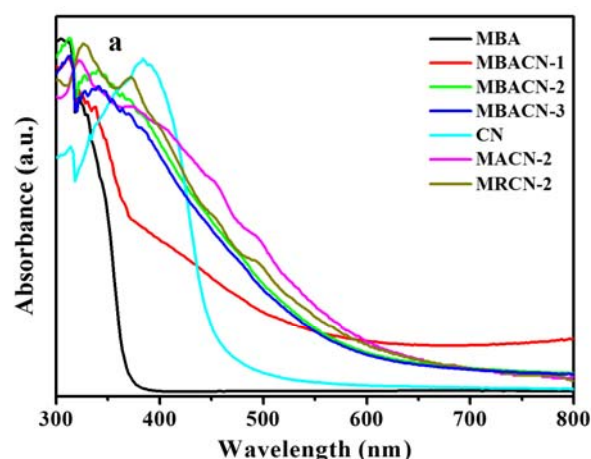

Fig. 4 a) UV-visible absorbance of MBA, MBACN-x, CN, MACN-2, and MRCN-2. b) PL spectra for MBA, MBACN-2, MACN-2, MRCN-2, and CN.

of anatase in this process, and the benefit of including a brookite phase.[42]

The photocatalytic activity of the different samples under visible light irradiation was investigated by degrading phenol (Fig. 5); CN was treated as a reference material for the composites. The photocatalytic degradation was fitted to pseudo-first-order kinetics, and the apparent rate constant, k, was equal to the corresponding slope of the fitted line. In Fig. 5a, MBA showed negligible photoactivity, while all of composites, which incorporated g-C$_3$N$_4$, exhibited higher activity than CN. The best performing sample, MBACN-2, degraded phenol with a reaction rate constant of 4.1×10^{-3} min^{-1}, an approximately 5-fold increase over CN. Compared to the brookite-containing TiO$_2$ (MBACN-x) hollow spheres, composite g-C$_3$N$_4$ and anatase TiO$_2$ (MACN-2) or rutile TiO$_2$ (MRCN-2) hollow microspheres had much lower levels of photoactivity
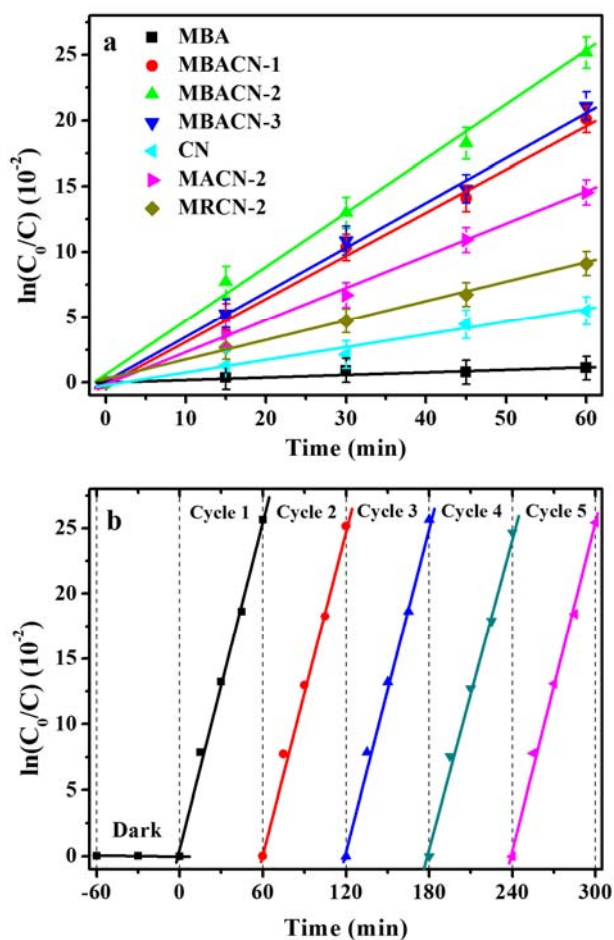
Fig. 5 a) Photocatalysis of phenol over MBA, MBACN-*x*, CN, MACN-2, and MRCN-2 under visible light irradiation. b) Recycling test of the MBACN-2 photocatalyst. The system was kept in the dark prior to testing.

Fig. 6 Comparisons between photocatalytic degradation of MBACN-*x* with and without a) the radical scavenger *t*-BuOH or b) the hole scavenger EDTA-2Na.

(Table S1). As shown in Fig. 5b, there was negligible adsorption of phenol in the dark, and only a slight decrease of activity resulted after repeating 4 times. The morphological stability of MBACN-2 was investigated by SEM and little change was observed after the 5 cycles, demonstrating excellent mechanical durability of the mesoporous composite microspheres (Fig. S7a and b). Further characterization by XRD and XPS confirmed that no obvious changes in crystallinity, chemical composition and bonding states occurred during the 5 cycles (Fig. S7c-f). XPS of MBACN-2 is discussed in detail below.

The enhanced photoactivity of MBACN-*x* was ascribed to the presence of hybrid brookite/anatase TiO_2 that enabled formation of the tricomponent brookite/anatase TiO_2/g-C_3N_4 heterojunction, which led in turn to higher visible light absorption and a lower band gap energy. Moreover, the mesoporous structure derived from the TiO_2 nanosheets provided efficient pathways for mass transfer. The phenol molecules could adsorb onto the g-C_3N_4 surface with offset face-to-face orientation via π–π conjugation, which accelerated the degradation. The hollow spherical morphology built by the nanosheet can enhance mass diffusion while possibly reflecting light inside of the composite capsules.

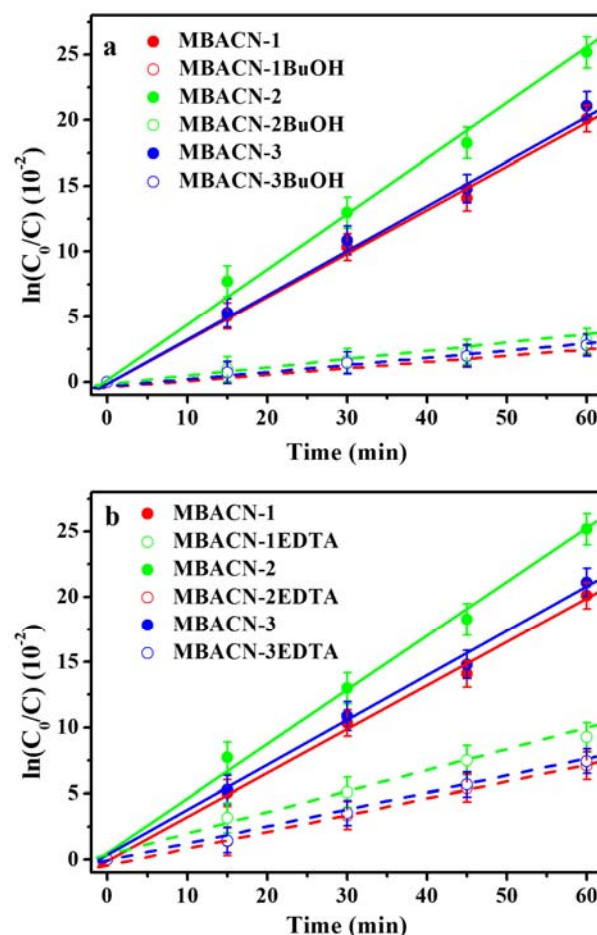To detect the main oxidation species involved in photodegradation, trapping experiments were conducted to

scavenge the hydroxyl radicals generated from photoexcited electrons and holes. *t*-BuOH was used as a radical scavenger (Fig. 6a), while EDTA-2Na was a hole scavenger (Fig. 6b). In the presence of *t*-BuOH, the photocatalytic activity of MBACN-*x* was effectively suppressed, implying that a considerable amount of photogenerated electrons were involved in photocatalysis under visible light irradiation, especially for MBACN-2. In contrast, the addition of EDTA-2Na caused less of a decrease with MBACN-*x*, indicating that photogenerated holes were not the main species responsible for phenol photodegradation.

XPS was conducted to investigate the chemical composition and bonding states of MBACN-2, as well as the VB edges of MBA and all MBACN-*x* samples (Fig. 7). The titanium spectra in Fig. 7a showed two main Ti 2p peaks centred at binding energies of 458.6 eV and 464.3 eV, which were assigned to the Ti 2p 3/2 and Ti 2p 1/2 of TiO_2.[43] The carbon spectra were fitted to three major peaks (Fig. 7b), with binding energies located at 284.6 eV, 286.3 eV, and 288.1 eV. These were assigned respectively to graphitic carbon, C-N coordination between aromatic rings, and N-C=N coordination in the *s*-triazine aromatic ring attached to NH_2 groups.[26] The nitrogen spectra showed three separated peaks centred at 398.9 eV, 400.1 eV, and 401.3 eV (Fig. 7c), which were assigned to N-C bonds between aromatic rings, C=N-C coordination in an aromatic ring, and amino groups at the
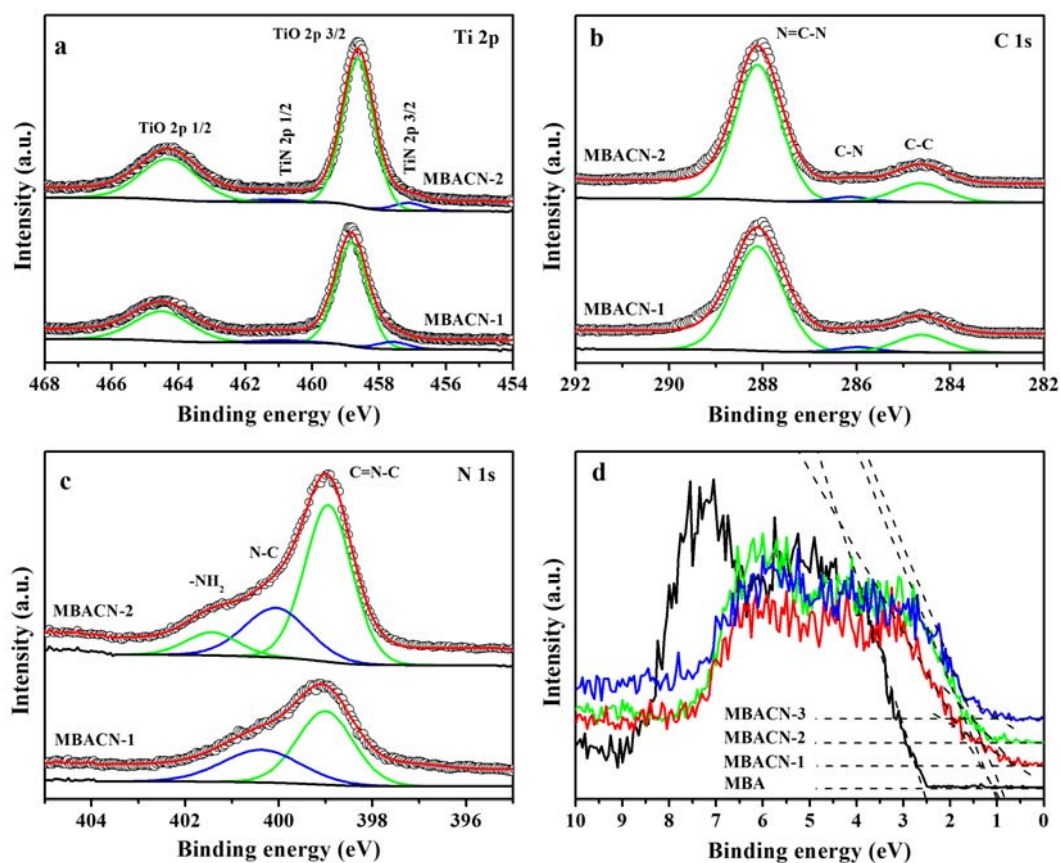
Fig. 7 XPS of MBACN-2: a) Ti 2p, b) C 1s and c) N 1s. d) VB XPS of MBA and MBACN-x. The curves of MBACN-x were shifted up the intensity axis to distinguish the band edge.

edge, respectively.[26] The VBs of MBA, MBACN-1, MBACN-2, and MBACN-3 were determined from Fig. 7d, with band edges of 2.60 eV, 1.36 eV, 1.29 eV, and 1.51 eV, respectively. Thus, the presence of g-C_3N_4 in the MBACN-x composites shifted the main absorption onset to a lower binding energy (relative to MBA which lacked the g-C_3N_4 layer) due to crystal defects derived from the TiO_2/g-C_3N_4 interface. These defects were caused by N atoms (from g-C_3N_4) which substituted for O atoms on the interface when the heterojunction formed during the calcination of cyanamide adsorbed on the TiO_2 surface.[44-46]

To evaluate the brookite/anatase TiO_2 heterojunction in MBA, EPR, which is highly sensitive to paramagnetic species containing unpaired electrons, was used to detect the existence of Ti^{3+} defects (Fig. S8).[47] Pristine anatase TiO_2 (MA) shows an EPR signal centred at the g value of 1.994, indexed to Ti^{3+} in crystalline anatase, while rutile TiO_2 (MR) produced only a negligible peak due to fewer defects being present after high temperature calcination. Remarkably, a strong paramagnetic signal peak was detected in the mixed phase sample (MBA) at the g value of 1.998, implying efficient electron generation and separation through the interface.[48] Therefore, a proposed mechanism for charge transfer through the brookite/anatase TiO_2/g-C_3N_4 heterojunction during phenol degradation is shown in Scheme 2. The heterojunction was formed during the thermal polymerization of the pre-infiltrated cyanamide on the hybrid TiO_2 surface, followed by conversion to a thin, homogeneous g-C_3N_4 layer by calcination. Different to pristine g-C_3N_4, the g-C_3N_4
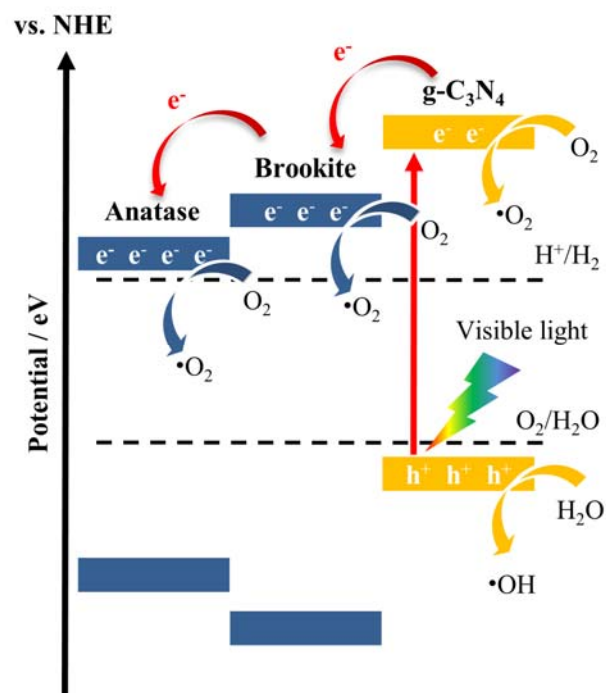
Scheme 2. A proposed mechanism for charge transfer through the heterojunction at the brookite/anatase TiO_2/g-C_3N_4 interface under visible light irradiation.

coating layer was partially confined along the walls of the TiO_2 nanosheets forming TiO_2/g-C_3N_4 core-shell structures. Visible light was harvested by the g-C_3N_4 shell, with photogenerated electrons in the CB of g-C_3N_4 transferring to the CB of brookite TiO_2 through the interface, then to the lower CB of anatase TiO_2, resulting in the separation of charge carriers. Furthermore, excited electrons located in the CBs of brookite/anatase TiO_2 and g-C_3N_4 can both convert O_2 to oxygen radicals for phenol oxidation, while phenol molecules were also degraded by hydroxyl radicals derived from holes in the VB of g-C_3N_4. Thus, the heterojunction formed at the hybrid TiO_2/g-C_3N_4 interface that enabled an elevated response to visible light, combined with the spherical hollow structure built of mesoporous nanosheets that provided for efficient light harvesting and excellent mass transfer, led to the high photocatalytic activity of the final MBACN-x composites. Compared with anatase TiO_2/g-C_3N_4 hollow microspheres, hybrid TiO_2/g-C_3N_4 microspheres of similar morphology have demonstrated more efficient charge transfer through brookite/anatase TiO_2 and TiO_2/g-C_3N_4 interfaces, resulting in an excellent visible photocatalytic performance.

Conclusions

Mesoporous brookite/anatase TiO_2/g-C_3N_4 hollow microspheres were fabricated by nanocoating pristine TiO_2 hollow microspheres with an aqueous cyanamide solution that was thermally converted to g-C_3N_4. The composite hollow microspheres featured numerous brookite/anatase TiO_2/g-C_3N_4 heterojunctions while maintaining the initial TiO_2 nanosheet structure after calcination. The photocatalytic activity under visible light of the best performing composite, MBACN-2, was 5-fold higher than mesoporous g-C_3N_4, with this improvement due to a 9.8 wt% g-C_3N_4 coating on the TiO_2 substrate. Despite being coated with g-C_3N_4, the MBACN-2 hollow microspheres remained mesoporous with reasonable surface area (37.1 m^2 g^{-1}) and pore volume (0.20 cm^3 g^{-1}). The mesoporous brookite/anatase TiO_2/g-C_3N_4 microspheres that are photoactive under visible light demonstrate great potential for decomposing organic pollutants for environmental remediation.

Conflicts of interest

There are no conflicts to declare.

Acknowledgements

Notes and references

1. X. B. Chen and S. S. Mao, *Chem. Rev.*, 2007, **107**, 2891.
2. D. Yang, H. Liu, Z. Zheng, Y. Yuan, J. Zhao, E. R. Waclawik, X. Ke and H. Zhu, *J. Am. Chem. Soc.*, 2009, **131**, 17885.
3. D. Yang, S. Sarina, H. Zhu, H. Liu, Z. Zheng, M. Xie, S. V. Smith and S. Komarneni, *Angew. Chem., Int. Ed.*, 2011, **50**, 10594.
4. Y. Ma, X. L. Wang, Y. S. Jia, X. B. Chen, H. X. Han and C. Li, *Chem. Rev.*, 2014, **114**, 9987.
5. S. Zhang, H. Yang, H. Huang, H. Gao, X. Wang, R. Cao, J. Li, X. Xu and X. Wang, *J. Mater. Chem. A*, 2017, **5**, 15913.
6. A. L. Linsebigler, G. Q. Lu and J. T. Yates, *Chem. Rev.*, 1995, **95**, 735.
7. A. Di Paola, M. Bellardita and L. Palmisano, *Catalysts*, 2013, **3**, 36.
8. B. Zhao, F. Chen, Q. W. Huang and J. L. Zhang, *Chem. Commun.*, 2009, **34**, 5115.
9. A. Pottier, C. Chaneac, E. Tronc, L. Mazerolles and J. P. Jolivet, *J. Mater. Chem.*, 2001, **11**, 1116.
10. T. A. Kandiel, A. Feldhoff, L. Robben, R. Dillert and D. W. Bahnemann, *Chem. Mater.*, 2010, **22**, 2050.
11. X. B. Chen, S. H. Shen, L. J. Guo and S. S. Mao, *Chem. Rev.*, 2010, **110**, 6503.
12. X. B. Chen, L. Liu, P. Y. Yu and S. S. Mao, *Science*, 2011, **331**, 746.
13. H. Yamashita, M. Harada, J. Misaka, M. Takeuchi, B. Neppolian and M. Anpo, *Catal. Today*, 2003, **84**, 191.
14. R. Asahi, T. Morikawa, T. Ohwaki, K. Aoki and Y. Taga, *Science*, 2001, **293**, 269.
15. J. Wang, N. Tafen de, J. P. Lewis, Z. Hong, A. Manivannan, M. Zhi, M. Li and N. Wu, *J. Am. Chem. Soc.*, 2009, **131**, 12290.
16. P. Wang, X. Li, J. Fang, D. Li, J. Chen, X. Zhang, Y. Shao and Y. He, *Appl. Catal. B-Environ.*, 2016, **181**, 838.
17. D. J. Yang, J. Zhao, H. W. Liu, Z. F. Zheng, M. O. Adebajo, H. X. Wang, X. T. Liu, H. J. Zhang, J. C. Zhao, J. Bell and H. Y. Zhu, *Chem. Eur. J.*, 2013, **19**, 5113.
18. H. Liu, Z. Zheng, D. Yang, X. Ke, E. Jaatinen, J. C. Zhao and H. Y. Zhu, *ACS Nano*, 2010, **4**, 6219.
19. Y. Zhu, J. Ren, X. Yang, G. Chang, Y. Bu, G. Wei, W. Han and D. Yang, *J. Mater. Chem. A*, 2017, **5**, 9952.
20. S. Zhang, H. Yang, H. Gao, R. Cao, J. Huang and X. Xu, *ACS Appl. Mater. Interfaces*, 2017, **9**, 23635.

21. L. Cao, D. H. Chen and R. A. Caruso, *Angew. Chem., Int. Ed.*, 2013, **52**, 10986.

22. C. Wang, X. Zhang, Y. Zhang, Y. Jia, B. Yuan, J. Yang, P. Sun and Y. Liu, *Nanoscale*, 2012, **4**, 5023.

23. J. Ran, G. Gao, F. T. Li, T. Y. Ma, A. Du and S. Z. Qiao, *Nat. Commun.*, 2017, **8**, 13907.

24. J. Ran, B. Zhu and S. Z. Qiao, *Angew. Chem., Int. Ed.*, 2017, **56**, 10373.

25. X. C. Wang, K. Maeda, A. Thomas, K. Takanabe, G. Xin, J. M. Carlsson, K. Domen and M. Antonietti, *Nat. Mater.*, 2009, **8**, 76.

26. S. Cao, J. Low, J. Yu and M. Jaroniec, *Adv. Mater.*, 2015, **27**, 2150.

27. S. Zhang, H. Gao, X. Liu, Y. Huang, X. Xu, N. S. Alharbi, T. Hayat and J. Li, *ACS Appl. Mater. Interfaces*, 2016, **8**, 35138.

28. X. X. Zou, G. D. Li, Y. N. Wang, J. Zhao, C. Yan, M. Y. Guo, L. Li and J. S. Chen, *Chem. Commun.*, 2011, **47**, 1066.

29. J. G. Yu, S. H. Wang, J. X. Low and W. Xiao, *Phys. Chem. Chem. Phys.*, 2013, **15**, 16883.

30. L. Zhang, D. Jing, X. She, H. Liu, D. Yang, Y. Lu, J. Li, Z. Zheng and L. Guo, *J. Mater. Chem. A*, 2014, **2**, 2071.

31. C. Han, Y. D. Wang, Y. P. Lei, B. Wang, N. Wu, Q. Shi and Q. Li, *Nano. Res.*, 2015, **8**, 1199.

32. R. Zhu, C. Y. Jiang, B. Liu and S. Ramakrishna, *Adv. Mater.*, 2009, **21**, 994.

33. G. Liu, Y. N. Zhao, C. H. Sun, F. Li, G. Q. Lu and H. M. Cheng, *Angew. Chem., Int. Ed.*, 2008, **47**, 4516.

34. D. J. Yang, C. C. Chen, Z. F. Zheng, H. W. Liu, E. R. Waclawik, Z. M. Yan, Y. N. Huang, H. J. Zhang, J. C. Zhao and H. Y. Zhu, *Energ. Environ. Sci.*, 2011, **4**, 2279.

35. D. Dambournet, I. Belharouak, J. Ma and K. Amine, *J. Mater. Chem.*, 2011, **21**, 3085.

36. M. Zhao, H. Xu, H. Chen, S. Ouyang, N. Umezawa, D. Wang and J. Ye, *J. Mater. Chem. A*, 2015, **3**, 2331.

37. H. Wei, W. A. McMaster, J. Z. Y. Tan, L. Cao, D. Chen and R. A. Caruso, *J. Phys. Chem. C*, 2017, **121**, 22114.

38. D. H. Chen, L. Cao, F. Z. Huang, P. Imperia, Y. B. Cheng and R. A. Caruso, *J. Am. Chem. Soc.*, 2010, **132**, 4438.

39. X. F. Chen, Y. S. Jun, K. Takanabe, K. Maeda, K. Domen, X. Z. Fu, M. Antonietti and X. C. Wang, *Chem. Mater.*, 2009, **21**, 4093.

40. Y. J. Wang, R. Shi, J. Lin and Y. F. Zhu, *Energy Environ. Sci.*, 2011, **4**, 2922.

41. B. Jurgens, E. Irran, J. Senker, P. Kroll, H. Muller and W. Schnick, *J. Am. Chem. Soc.*, 2003, **125**, 10288.

42. X. F. Chen, J. Wei, R. J. Hou, Y. Liang, Z. L. Xie, Y. G. Zhu, X. W. Zhang and H. T. Wang, *Appl. Catal. B-Environ.*, 2016, **188**, 342.

43. N. Daude, C. Gout and C. Jouanin, *Phys. Rev. B*, 1977, **15**, 3229.

44. X. B. Chen and C. Burda, *J. Am. Chem. Soc.*, 2008, **130**, 5018.

45. A. Sinhamahapatra, J. P. Jeon and J. S. Yu, *Energy Environ. Sci.*, 2015, **8**, 3539.

46. X. Y. Xin, T. Xu, J. Yin, L. Wang, C. Y. Wang, *Appl. Catal. B: Environ.*, 2015, **176-177**, 354.

47. C. P. Kumar, N. O. Gopal, T. C. Wang, M.-S. Wong and S. C. Ke, *J. Phys. Chem. B.*, 2006, **110**, 5223.

48. S. M. El-Sheikh, G. Zhang, H. M. El-Hosainy, A. A. Ismail, K. E. O'Shea, P. Falaras, A. G. Kontos and D. D. Dionysiou, *J. Hazard. Mater.*, 2014, **280**, 723.

TOC Graphic and text
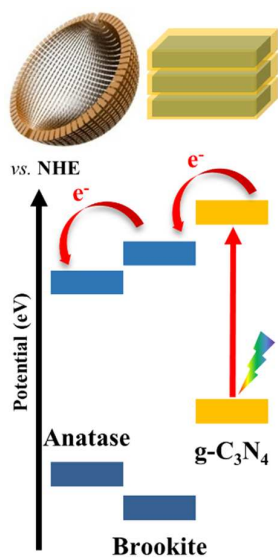
Improving photocatalytic performance under visible light irradiation by using multicomponent heterojunctions.